Supplementary materials

Bridging in co-cured composite joints

Charline van Innis[1*], Michal K. Budzik[2], Thomas Pardoen[1,3]

[1]*Institute of Mechanics, Materials and Civil Engineering (iMMC), UCLouvain, Louvain-la-Neuve, Belgium (charline.vaninnis@uclouvain.be , thomas.pardoen@uclouvain.be)*

[2]*Department of Mechanical and Production Engineering (MPE), Aarhus University, Aarhus, Denmark (mibu@mpe.au.dk)*

[3]*Wel Research Institute, avenue Pasteur, 6, 1300 Wavre, Belgique*

**Corresponding author: charline.vaninnis@uclouvain.be*

S1 Supplementary material 1: Influence of PEI thickness on G_{Ic} of co-cured joints

S2 Supplementary material 2: Analytical bridging model

S3 Supplementary material 3: Relative toughening effect number

S4 Supplementary material 4: Identification of fitting parameters of experimental results

A. S1: Influence of PEI thickness on G_{Ic} of co-cured joints

Owing to the lower mode I fracture toughness of adhesive co-cured composite joints with respect to secondary bonded joints, Quan and co-workers (Quan et al., 2023, 2022) suggested to replace the adhesive by a thermoplastic film such as polyetherimide (PEI) as interactions between PEI and epoxy results in a morphological gradient as the one shown in Figure S1.1 . They inserted PEI films of varying thicknesses between composite pre-pregs made of the 8552 epoxy resin. They reported a larger mode I fracture toughness compared to composite delamination but lower than compared to secondary bonded joints. In addition, they reported an increase in G_{Ic} with the PEI film thickness with an optimum thickness around 200 µm. To our knowledge, co-curing of composite joints using a PEI film has never been performed through the resin transfer moulding (RTM) process. In the case of pre-pregs, the carbon fabric plies are already impregnated by the resin leading to a resin layer between the PEI film and the carbon fibres before curing. Opposite, in RTM, the carbon fibres are in contact with the PEI film and the resin is then injected. Hence, the fibres can remain in contact with the PEI films. This work investigated the toughness of co-cured composite joints through RTM and the influence of the PEI film thickness on G_{Ic} and the failure mechanisms taking place.

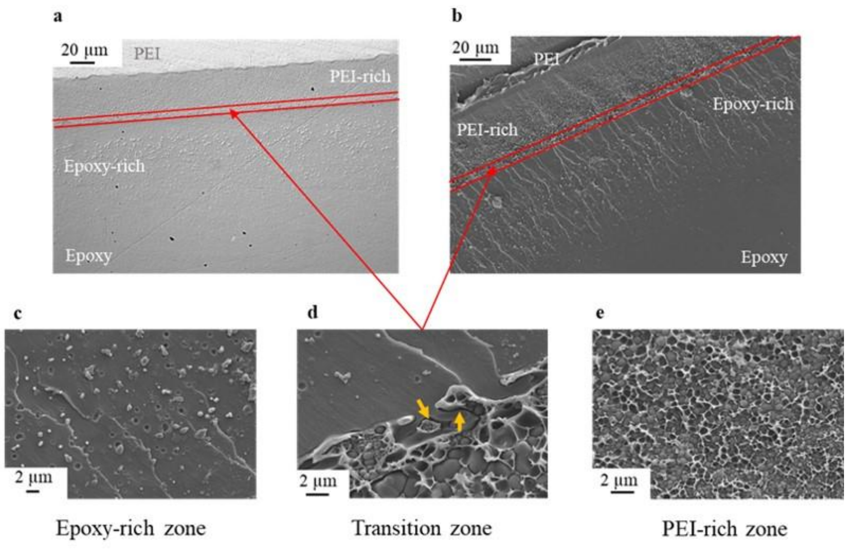

Figure S1.1: a) Optical and b) SEM micrographs of the PEI-epoxy interphase with c) the epoxy-rich zone exhibiting a sea-island morphology, d) the transition zone and e) the PEI-rich zone characterized by a nodular morphology.

1. Materials and methods

1.1.Joints manufacturing

A PEI (Ultem 1000, Sabic) is inserted between Hexforce G0926 carbon fibres fabrics (5 at each side). At one side of the PEI film, two Kapton films (Dupont) are inserted to introduce a pre-crack. The stack is inserted in the RTM mould closed with 8 bars press. The Hexflow RTM6 resin is then injected at a temperature of 90°C until reaching a pressure of 6 bars in the mould. The composite is then cured following the optimized curing cycle for PEI-RTM6 interphase developed by Voleppe et al. (Voleppe et al., 2021). The temperature is increased at a rate of 2°C/min up to 160°C for 90 min. Finally, the temperature is increased up to 180°C at a rate of 2°C/min and the temperature plateau is maintained for two hours. 50 µm and 175 µm thick PEI films have been used. Composite parts without PEI film have been manufactured to determine the delamination G_{Ic} of the composite as reference.

1.2.Mechanical testing

The DCB samples, shown in Figure 3a, have been machined from the cured panels with a length of 200 mm and a width of 20 mm in a direction such that the fishing lines are aligned perpendicular to the crack propagation direction. The 70 mm long Kapton film inserted to create the pre-crack results in initial crack length of 50 mm. The total height of the samples is about 4 mm. The DCB tests are performed following the ISO 25217 standard on a Zwick/Roell machine equipped with a 50 kN loadcell, at constant crosshead speed of 1 mm/min. The machine is located in a ventilated room at constant temperature and relative humidity content about 23°C and 50%, respectively. Prior to testing, the edge of the samples is graduated to determine the crack length. The crack is tracked using a Canon EOS1400D camera taking pictures every 3 seconds. G_{Ic} is then computed following the beam bending theory.

1.3.Microscopy

Scanning electron microscopy (SEM) with Ultra 55 Field-Emission SEM (Zeiss, Germany) under 5 keV and optical microscopy with a Provis AX70 microscope from Olympus has been used for fractography analyses. This required cutting joints along the crack propagation direction and polishing the cross-section prior characterization.

2. Results and discussion

2.1.Co-cured composite joints with PEI

Figure S1.2 shows the R-curves resulting from the DCB testing of the composite parts and the PEI co-cured joints. Inserting a 50 µm thick PEI film results in a fracture toughness about 284 ± 89 J/m² while a 175 µm thick film results in a lower G_{Ic} about 146 ± 28 J/m². A delaminating composite is characterized by a G_{Ic} about 359 ± 109 J/m². In average, inserting a 50 µm thick PEI film results in a lower G_{Ic} compared to composite delamination but some points are competitive with composite delamination. The 175 µm always leads into a lower fracture toughness compared to the reference composite.

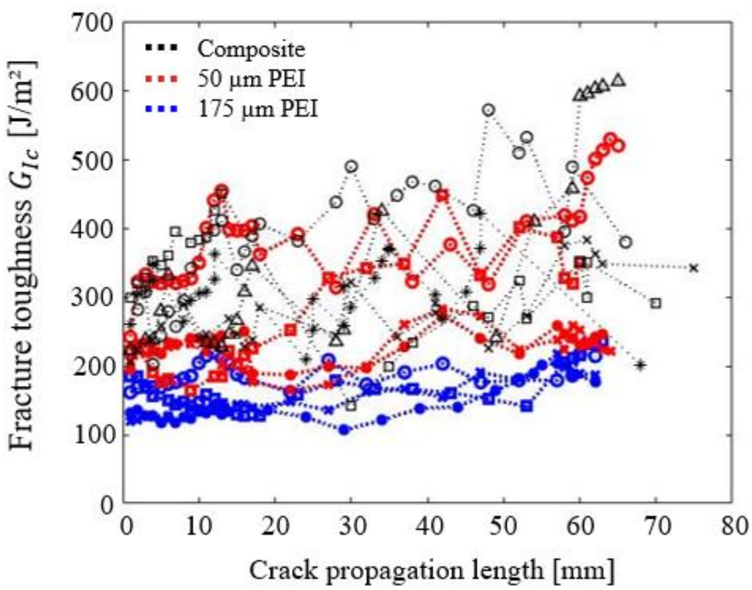

Figure S1.2: R-curves for the composite delamination (black), the co-cured composite joints with a PEI a 50 µm (red) and a 175 µm (blue) thick film.

Figure S1.3 shows the failure mechanisms taking place in co-cured composite joints with a 50 µm thick PEI film. Due to the architecture of the carbon fibres plies, the crack can propagate in resin-rich pockets or along carbon fibres. Upon curing, a morphological gradient as reported by Voleppe et al. (Voleppe et al., 2021) develop. At the locations of the resin-rich pockets (Figure S1.3b-e), this gradient can fully develop and the crack propagates along the interface between the resin and PEI-rich zones (Figure S1.3d). Sometimes, it is also slightly deflected into the PEI-rich zone (Figure S1.3e). In the second case, the crack propagates away of a resin pocket (Figure S1.3f-i). The crack can propagate through the PEI film (Figure S1.3f and g) generating some short bridging PEI ligaments and some local mode-mixity due to the deflection. If it does not propagate through the film, it propagates along the carbon fibres located in the PEI-rich zone owing to the development of the morphological gradient (Figure S1.3h and i).

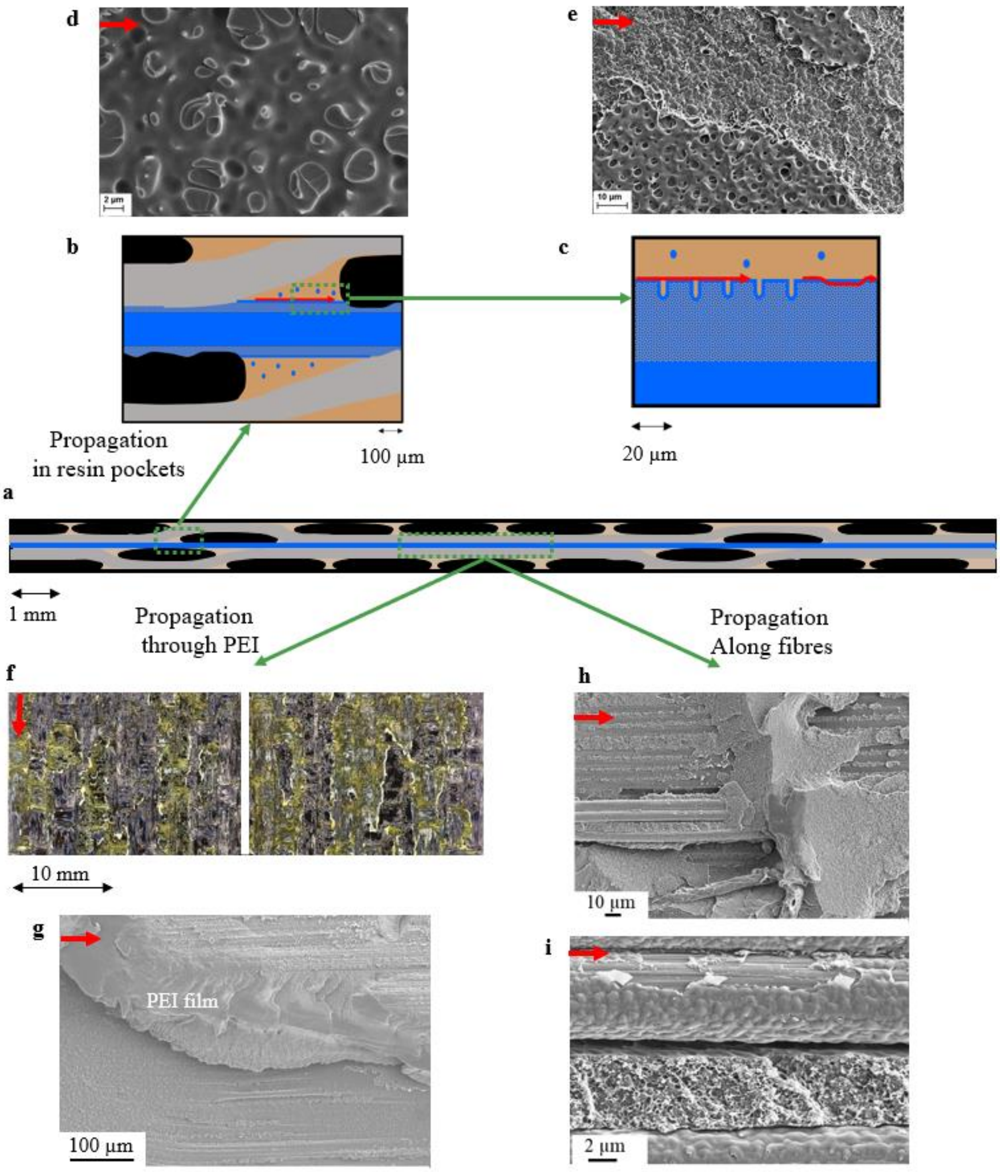

Figure S1.3: *Failure mechanisms taking place in co-cured composite joints with a 50 µm thick PEI film: a) scheme of the joint, b) morphological gradient in a resin pocket and c) zoom on the PEI-rich/epoxy-rich interface where the crack propagates d) along the PEI-rich/epoxy-rich interface or e) locally in the PEI-rich zone, f) fracture surface with PEI on both side indicating g) propagation through the PEI film. H) Propagation along the fibres present in the PEI-rich zone away of the resin pockets. The red arrows indicate the crack propagation direction.*

Figure S1.4 shows the failure mechanisms taking place in co-cured composite joints with a 175 µm thick PEI film. In this case, the crack is no longer able to propagate through the PEI film as shown in Figure S1.4a. As with the 50 µm thick PEI film, in resin-rich pockets, the crack propagates along the interface between the PEI-rich and epoxy-rich zones of the morphological gradient (Figure S1.4c-d). Away from the resin pockets, crack propagation takes place along the fibres in the PEI-rich zone (Figure S1.4e-f). Opposite to the present results, in adhesive joints, an increase in G_{Ic} is reported with the adhesive thickness and the same behaviour was found increasing the PEI film thickness between 90 and 250 µm. Hence, it is believed that the higher toughness resulting from the insertion of a 50 µm PEI film originates from the crack deflection through the PEI film that results in some mode-mixity at the crack tip and in the formation of small PEI bridging ligaments. Crack deflection (Reedy, 2008) and bridging (Quan et al., 2020) are two well-known toughening mechanisms in adhesive joints.

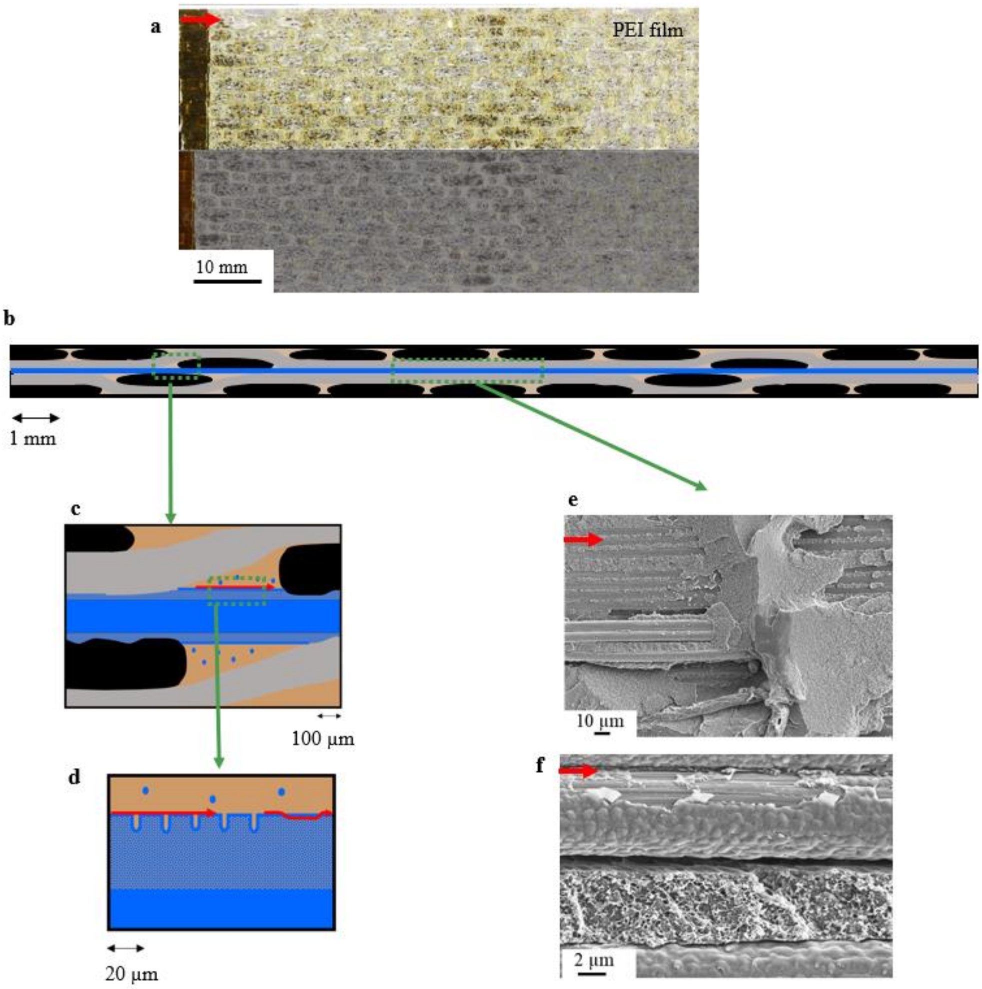

Figure S1.4: Failure mechanisms taking place in co-cured composite joints with a 175 µm thick PEI film: a) whole fracture surfaces with the PEI film remaining only on one face, b) scheme of the composite (PEI in blue), c-d) propagation in resin rich pockets where d) the morphological gradient develops and d) the crack propagates along the PEI-rich/epoxy-rich interface or slightly in the PEI-rich zone, e) propagation along the fibres in f) the PEI-rich zone. The red arrows indicate the crack propagation direction.

Opposite to the results of Quan and co-workers (Quan et al., 2023, 2022), inserting a PEI film results in a lower G_{Ic} as the one of the reference composites. Along the fibres, delamination in the PEI-rich zone was also reported. However, crack propagation along the PEI-rich and epoxy-rich interface and through the PEI film were not reported by Quan et al. Propagation through the film cannot explain the lower G_{Ic} while the propagation along the interface could but this mechanism only takes place very locally and cannot explain such a significant difference. Another factor can be the combination between the PEI film and the epoxy resin. In the work of Quan et al., the 8552 resin is harder than the PEI while in the present case, the RTM6 is softer. In the work of Quan et al., the PEI layer can thus act as a dissipative layer (Bertholet et al., 2007; Dépinoy et al., 2019). In addition, the 8552 resin is toughened by a thermoplastic and the enzyme coating of the fibres could be adapted to this particularity while not for the present used carbon fibres resulting in a weaker interface with the carbon fibres, decreasing the toughness.

2.2.Co-cured composite joints with PEI and fishing lines

In order to determine if the addition of fishing lines could be beneficial to the joint toughness, fishing lines spaced by 5 mm have been inserted at both sides of 50 and 175 µm thick PEI films prior to co-curing. The fishing lines were deposited one by one and when there coated with resin to prevent their motion. The resulting R-curves are shown in Figure S1.5. Inserting fishing lines in the joint joints with the 50 µm film results in a steady-state fracture toughness about 837 ± 50 J/m² which represent an increase by a factor 2.9. If fishing lines are inserted with the 175 µm thick film, G_{Ic} is about 464 ± 55 J/m², an increase by a factor 3.1 compared to the joint without fishing lines. This toughening originates from the fishing lines acting as bridging ligaments behind the crack tip.

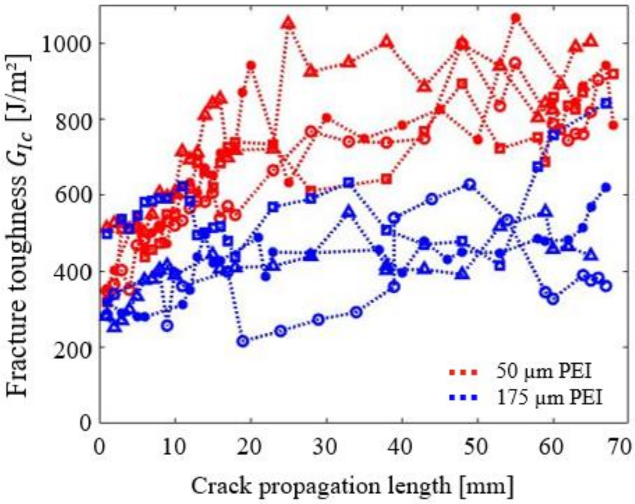

Figure S1.5: R-curves the co-cured composite joints with a PEI a 50 µm (red) and a 175 µm (blue) thick film in which fishing lines are inserted, spaced by 5 mm.

3. Conclusion of Supplementary Material 1

Inserting fishing lines into a co-cured composite joint with a PEI film results in toughening effect originating from the bridging induced by the fishing lines. No matter the thickness of the PEI film, the mode I fracture toughness is increased by a factor 3 by inserting fishing lines at both sides of the PEI film every 5 mm. For the following experiments, a 50 µm thick film has only be used as it leads to the highest fracture toughness. In addition, this could also lead to the strongest joint as the tensile and lap-shear strength of joints are known to decrease with the adhesive thickness. The joint containing a 50 µm thick film thus probably offers the trade-off in term of toughness, stiffness and strength.

B. S2 – Analytical bridging model

1. Governing equations

The considered configuration is the one of a double cantilever beam (DCB) of a thickness *2h*, width *B* and in which *a* crack of length a is present. In addition, toughening occurs by bridging due to the presence of *n* bridging ligaments spaced by a distance λ and that are placed at the L_i positions (i=1,2, …, n) as shown in Figure S2.1.

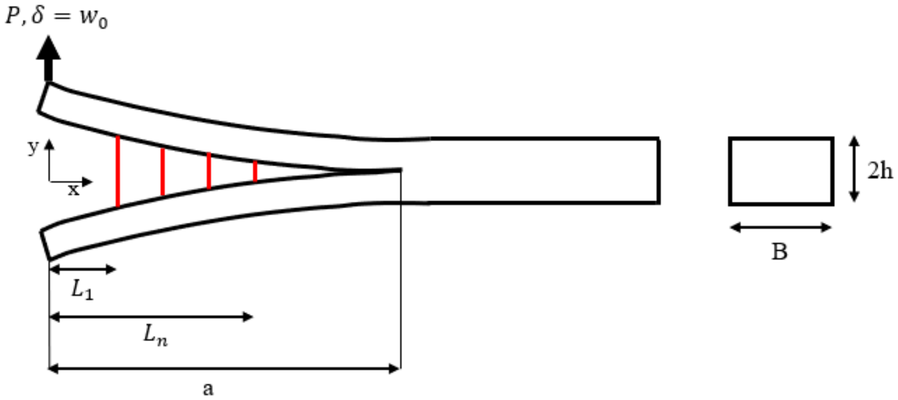

Figure S2.1: Double cantilever beam configuration with a width B, a height 2h. A crack of length a is present with n bridging filaments present in its wake, placed at the positions L_i*.*

When the DCB opens, the bridging filaments are deformed and carry each one a force F_i that depends on the beam deflection at the position $w_i(L_i)$ such that $F_i = F_i(w_i(L_i))$. This requires to define a bridging law (see section 3). The equations describing the beam deflection are first derived based on the Euler-Bernoulli beam theory. The relationship between the beam deflection and the load for a simple DCB is given by

$$\frac{\partial w^2}{\partial x^2} = -\frac{M}{EI} = \frac{Px}{EI}, \qquad (S2.1)$$

with *x* being the position along the DCB with the origin corresponding to the loading point, *M* the bending moment resulting from the applied load *P*. *E* is the beam Young's modulus and *I* is the second moment of inertia equal to $\frac{Bh^3}{12}$. If *n* bridging filaments are now considered, the deflection of the beam between two consecutive filaments located in L_i and L_{i+1} (i=1, 2, … n) is given by

$$\frac{\partial w^2}{\partial x^2} = -\frac{M}{EI} = \frac{Px - \sum_{j=1}^{i} F_i(x - L_j)}{EI} \quad \text{for } L_i \le \ x \le \ L_{i+1}. \qquad (S2.2)$$

This leads to an expression for $w_i(x)$, the beam deflection equation for $L_i \le \ x \le \ L_{i+1}$:

$$w_i(x) = \frac{Px^3}{6EI} - \sum_{j=1}^{i} \frac{F_j}{EI}\left(\frac{x^3}{6} - \frac{L_j x^2}{2}\right) + C_i x + D_i \,. \qquad (S2.3)$$

If *i* is set to 0, the second term is equal to 0 and the deflection and the loading point $\delta = w_0$ is determined. The boundary equations needed to determine the C_i and D_i constants are

$$\begin{cases} w_n(a) = 0 \\ \dfrac{\partial w_n(a)}{\partial x} = 0 \\ w_i(L_{i+1}) = w_{i+1}(L_{i+1}) \\ \dfrac{\partial w_i(L_{i+1})}{\partial x} = \dfrac{\partial w_{i+1}(L_{i+1})}{\partial x} \end{cases} . \qquad (S2.4)$$

The two first boundary conditions allow to determine the C_n and D_n coefficients of w_n such that $L_n \le x \le a$

$$C_n = -\frac{Pa^2}{2EI} + \sum_{j=1}^{n} \frac{F_j}{EI}\left(\frac{a^2}{2} - l_j a\right) , \qquad (S2.5)$$

$$D_n = -\frac{Pa^3}{6EI} - C_n a + \sum_{j=1}^{n} \frac{F_j}{EI}\left(\frac{a^3}{6} - \frac{L_j a^2}{2}\right) . \qquad (S2.6)$$

The two last boundary conditions provide a generic formula for the other C_i and D_i coefficients for i=0, 1, 2, … n-1. *i*= 0 corresponding to the deflection equation for $x \le L_1$.

$$C_i = C_{i+1} - \frac{F_{i+1} L_{i+1}^2}{2EI} , \qquad (S2.7)$$

$$D_i = D_{i+1} + (C_{i+1} - C_i)L_{i+1} + \frac{F_{i+1}L_{i+1}^3}{3EI}\ . \qquad (S2.8)$$

Equations S2.3, S2.5, S2.6 and S2.7 are used to compute the beam deflection at the position of each bridging filament. In order to determine the toughness by considering the action of the bridging filament, one needs a crack propagation criterion. The total toughness is given by

$$G_{total} = G_0 + G_{bridging} \qquad (S2.9)$$

with G_0 being the fracture toughness in the absence of the bridging filaments and $G_{bridging}$ the contribution of the bridging filaments behind the crack tip. The crack propagates when the crack driving force at the crack tip G_{tip} (Equation 10) is equal to G_0.

$$G_{tip} = \frac{1}{BEI}\left(Pa - \sum_{j=1}^{n} F_j\left(a - L_j\right)\right)^2 = G_0. \qquad (S2.10)$$

In order to determine the G_{tip}, P and the bridging forces F_j must be determined. Determining the F_j forces requires to determine the deflection of the DCB at the positions L_j, $w_j(L_j)$ as the bridging force and the deflection are linked together through the bridging law. A system of *n*+1 equations is obtained that can be solved using the Newton-Raphson method. The guess of iteration *k* is denoted $X_k = (W_{1k}, W_{2k}, \ldots, W_{nk}, P_k)$ with W_{ik} being the guess of iteration *k* for the deflection in L_i while P_k is the guess for the applied load. The guess for the next iteration *k+1* is given by

$$X_{k+1} = X_k + \frac{H(X_{k+1})}{H'(X_{k+1})}, \qquad (S2.11)$$

where *H* is a real-value function of X_k and *H’* is the Jacobian of *H*. *H* is given by

$$H(X_k) = \begin{pmatrix} W_{1k} - w_1(L_1) \\ W_{2k} - w_2(L_2) \\ \vdots \\ W_{kn} - w_n(L_n) \\ G_{tip} - G_0 \end{pmatrix}. \qquad (S2.12)$$

Convergence is achieved when the residuals $|X_{k+1} - X_k|$ are lower than a certain value ϵ. In the present case $|W_{ik+1} - W_{ik}| < 0.001$ and $|P_{k+1} - P_k| < 0.1$. This system of equation determines thus the applied load P, bridging forces and deflection at the bridging filaments positions when the crack propagates.

2. Bridging law

The bridging law relates the bridging force F_i to the deflection at the position of the bridging filament $w_i(L_i)$. The distance between the two DCB arms at the position L_i is equal to $2w_i$. Hence, the bridging law gives $F(2w_i)$. It is well known that the bridging law influences the predicted DCB response. For example, Spearing and Evans (Spearing and Evans, 1992) showed that if the area under the different bridging laws and the bridging filament ultimate tensile force (UTF) are kept constant, the final fracture toughness is also constant. They considered bridging laws corresponding to a perfectly plastic filament, a linear elastic filament and fiber pullout (softening). The increasing part of the R-curve is modified with the steady-state fracture toughness being reached first for the perfectly plastic law and then for the pull-out case and finally, the elastic filament. In addition, the perfectly elastic and plastic laws result in an exponential increase of the toughness as the crack propagates while the increase is smoother when considering fiber pull-out. Li et al. (Li et al., 2021) used a bilinear trapezoidal law and the showed that the filament ductility can influence the response by impacting the snap-back instability and the resulting total fracture toughness. Four types of behavior have been considered here and are shown in Figure S2.2.

i. The bridging filaments behave as springs (Figure S2.2a). Each one has a stiffness K and breaks when the applied force reaches the UTF F^f.

ii. The bridging filament is first unfolded and starts to be loaded under tension when it reaches a length l_0 and breaks when the tensile force is equal to F^f (Figure S2.2b).

iii. The bridging filament is attached to the DCB arms at the opposite interfaces close to the DCB edge. Depending on the radius of the bridging filament and the width of the DCB, tensile or bending conditions dominate (Figure S2.2c and e).

iv. The bridging filament is bonded to one arm except in one point where it is attached at the opposite interface and decohesion between the filament and the two adherents take place over a distance d. Depending on this distance and the filament radius, bending or tension dominates (Figure S2.2d and f).

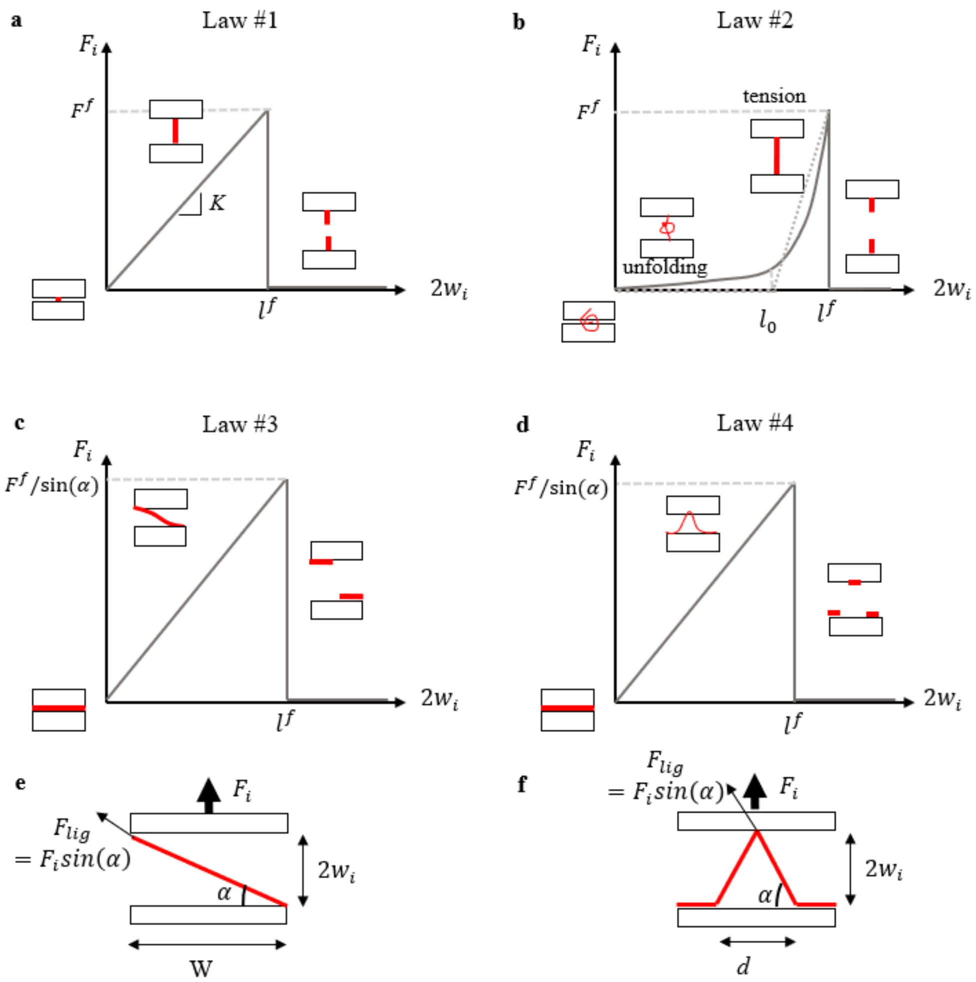

Figure S2.2: Bridging laws: a) the filament behaves as a spring, b) the filaments first unfold before being loaded under tension (dashed-curve: ideal case; plain curve: modelling), c) the filament is attached at the edges of the DCB, d) decohesion takes place over a short distance d while the debonded part adheres to the opposite interface. e-f) Bridging filament configuration for e) the law in c and f) the law in d.

2.1.Bridging law #1: springs (Figure S2.2a)

The bridging filaments act as springs. The force linearly increases with the applied displacement and they break when the applied force is equal to the bridging filament UTF F^f and when their final extension is equal to l^f. The stiffness of the filament is given by $K = F^f/l^f$. The bridging law is thus written as

$$F_i(2w_i) = \begin{cases} 2Kw_i & 0 \leq 2w_i \leq l^f \\ 0 & l^f \leq 2w_i \end{cases} . \qquad (S2.13)$$

2.2.Bridging law #2: elongation and tension (Figure S2.2b)

This bridging law considered that the bridging filament is loaded under tension when it has a length l_0 meaning that a bridging force is applied on the filament when $w_i \geq l_0$. For $w_i < l_0$, the filament is unfolded. The filament breaks when the applied force is equal to the bridging filament UTF F^f and when their final extension is equal to l^f. If the filament is perfectly elastic, l^f depends on the filament Young's modulus E^f and is given by $l^f = \left(1 + (F^f/AE^f)\right) l_0$ with *A* being the fishing line cross-section area. This would require to have a curve similar to the dashed one shown in Figure S2.2, but convergence issues appear due to the sharp increase in stiffness when $w_i = l_0$. Consequently, it is assumed that it slightly increases during unfolding and the ideal bridging law is approximated by an exponential function such that $F_i(w_i = l_0) < 0.1F^f$. The bridging law is thus given by

$$F_i(w_i) = \begin{cases} b_1 \exp(2b_2 w_i) & 0 \leq 2w_i \leq l^f \\ 0 & l^f \leq 2w_i \end{cases}, \qquad (S2.14)$$

with b_1 and b_2 being two fitting coefficients.

2.3.Bridging law #3: filament attached at opposite interface close to the edges (Figure S2.2c)

The bridging filament is considered to be attached to the DCB beams only at the edges of the DCB. Along the width of the DCB, decohesion takes place. Depending on the radius of the bridging filament and the width, bending or tension dominates. Under small deformation, the force required to bend the filament is given by

$$F_{bending}(L_i) = \frac{3E\pi r^4(2w_i)}{B^3}, \qquad (S2.15)$$

while the tensile force applied on the filament is given by

$$F_{tension}(L_i) = \frac{1 - \cos(\alpha)}{\cos(\alpha)\sin(\alpha)} E\pi r^2, \qquad (S2.16)$$

with α being the angle between the bridging filament and the DCB arm given by $\alpha = \text{atan}\,(2w_i/B)$. Figure S2.3 shows the evaluated $F_{bending}$ and $F_{tension}$ for several values of radius r and displacement values $2w_i$. The transition from the "tension dominated" mode to the "bending dominated" mode takes place when r/B is about 0.4 for small deflections and increases as the deflection increases. This transition ratio is independent on E^f which only affects the magnitude of $F_{bending}$ and $F_{tension}$.

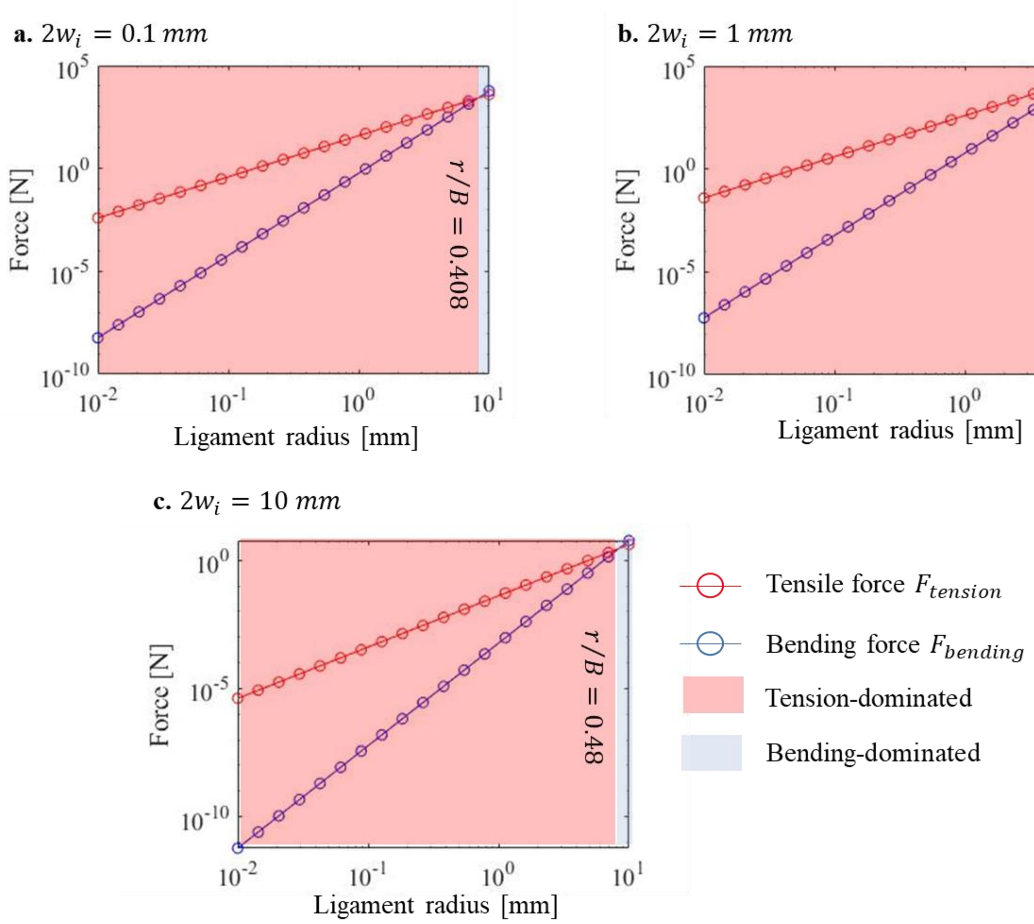

Figure S2.3: Variation of $F_{bending}$ and $F_{tension}$ for the bridging law #3 with the bridging filament radius for different displacements a. 0.1 mm, b. 1 mm and c. 10 mm. The width B is set to 20 mm and the filament Young's modulus to 5 GPa. The r/W ratio at which the transition from the tension-dominated regime to the bending dominated regime takes place is given in each graph.

Assuming that tension dominates (thin bridging filaments), it is possible to determine the force required to cause the filament failure so that $F_{tension}(w_i)\sin(\alpha) = F^f$ which also provides the beam deflection at failure l^f.

2.4.Bridging law #4: local decohesion (Figure S2.2d)

The fourth bridging law assumes that the bridging fiber debonds from the bottom arm over a distance *d* and is attached at its middle to the upper arm as shown in Figure S2.2d and f. Under small deformation, the force required to bend the bridging filament is given by

$$F_{bending}(L_i) = \frac{48E\pi r^4(2w_i)}{d^3} \ . \qquad (S2.17)$$

The force applied on the DCB if tension in the bridging filament dominates is given by

$$F_{tension}(L_i) = 2\frac{1-\cos(\alpha)}{\cos(\alpha)\sin(\alpha)}E\pi r^2 \ , \qquad (S2.18)$$

with $\alpha = \text{atan}\,(4w_i/d)$, the angle between the bridging filament and the bottom DCB arm. Figure S2.4 shows the evolution of $F_{bending}$ and $F_{tension}$ with the fiber radius and the displacement. It can be observed that the transition from a tensile-dominated regime to a bending-dominated regime always occurs for a r/d ratio about 0.2. If tension is assumed, the force required to apply failure can be determined based on $F_{tension}(w_i) = 2\sin(\alpha)F^f$ from which the deflection at failure l^f can be determined.

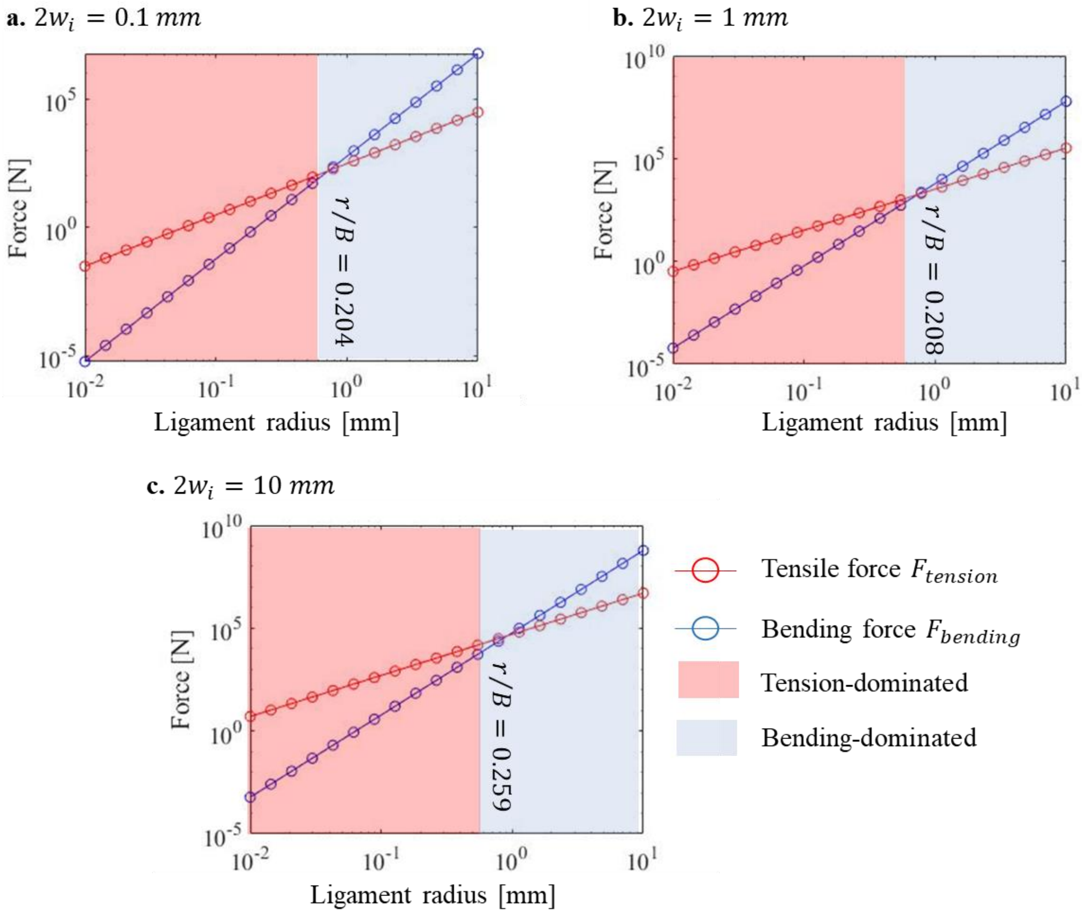

Figure S2.4: Variation of $F_{bending}$ and $F_{tension}$ for the bridging law# 4 with the bridging filament radius for different displacements a. 0.1 mm, b. 1 mm and c. 10 mm. The distance d is set to 5 mm and the filament Young's modulus to 5 GPa. The r/W ratio at which the transition from the tension-dominated regime to the bending dominated regime takes place is given in each graph.

3. Numerical algorithm

The algorithm is schematized in Figure S2.5. The inputs of the models are the DCB beam Young's modulus, thickness and width, the spacing between the bridging filaments λ, the initial crack length a_0 and the final crack length for computations a_{max}, the position of the first bridging filament L_1 and the joint toughness in the absence of bridging G_0. In addition, depending on the selected bridging law, several inputs can be required such as the filament Young's modulus, radius, UTF, tensile elongation or initial unfolded elongation. Then for each crack length a_m, the position of all potential bridging filaments L_i are determined based on L_1. The Newton-Raphson algorithm is then used to determine the macroscopic load P_m and the

$w_i(L_i)$ deflections such that $G_{tip} = G_0$. When it has converged, the algorithm checks if all filaments are still unbroken or not. If not, L_1 is modified such that it corresponds to the position of first intact filament. The same computations are performed for each a_m ranging from a_0 to a_{max}. Finally, knowing the macroscopic load P_m for each value of a_m, the toughness is computed based on the Euler-Bernoulli beam theory:

$$G_{Ic} = \frac{12P_m^2 a_m^2}{EB^2h^3} \,. \qquad (S2.19)$$

The equation used to compute the toughness has an influence on the R-curve. Li et al. compared the compliance method and the single beam theory. Using the compliance method, G_{Ic} is constant until the filament starts to be damaged and G_{Ic} increases until the filament breaks. Using the single beam theory, as soon as the filament is active, G_{Ic} increases until the filament fails.

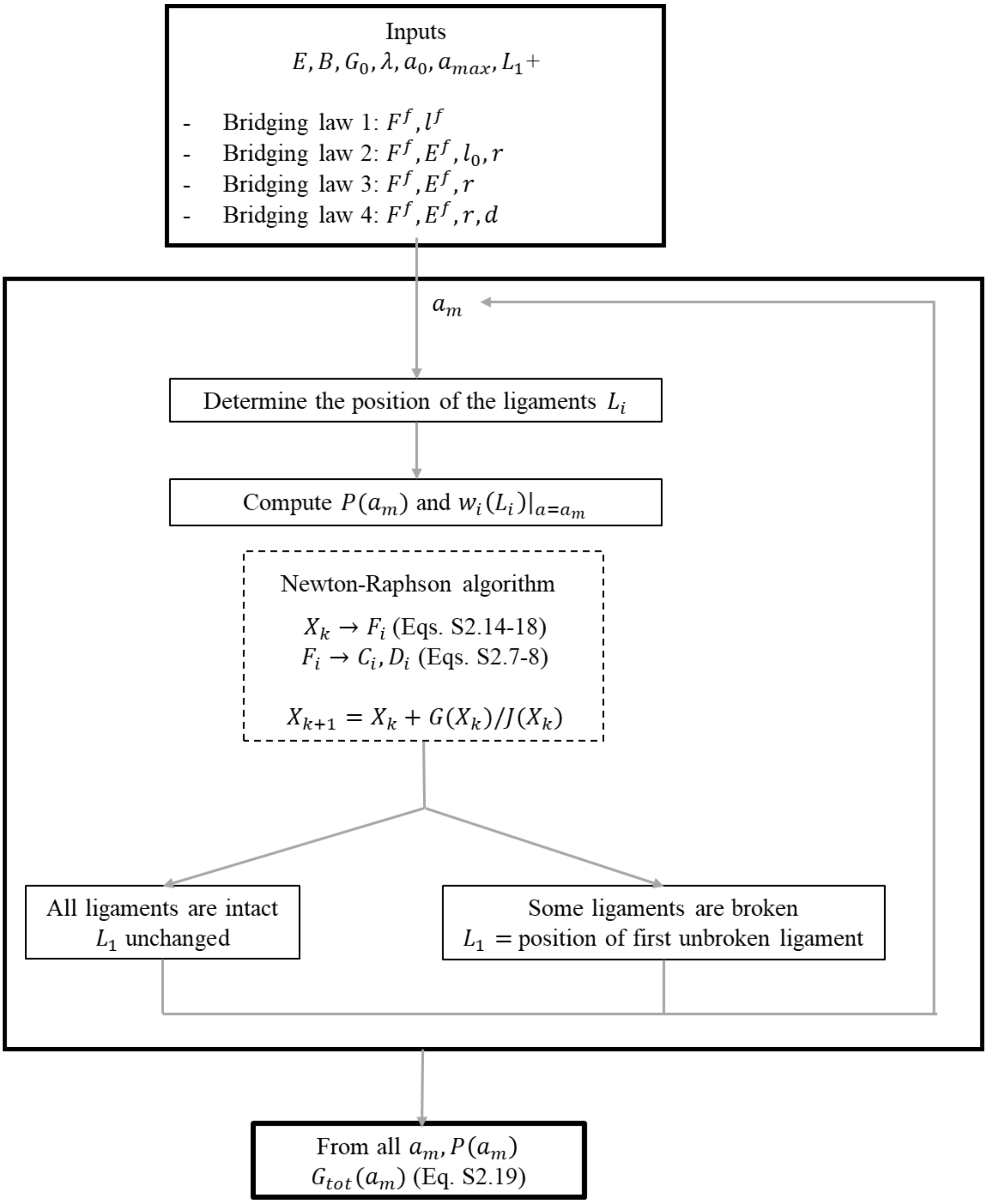

Figure S2.5: Algorithm for computing the joint fracture toughness considering the presence of bridging filaments.

4. Influence of the bridging law on the results

The four bridging laws introduced in section 2 are compared in term of the DCB response. However, one must determine how the different parameters will be adapted depending on the bridging law to obtain some equivalents. For this purpose, 5 cases have been analyzed and are given in Table S2.1. For every bridging law one considers a DCB having an initial crack length of 50 mm and the only considered bridging filament is located at a position $L_1 = 60$ mm.

Table S2.1: Parameters considered for the different cases to determine the influence of the bridging law and the resulting fracture toughness.

Case number	Law	Parameters	Energy to break one filament [mJ]	Maximum total fracture toughness
1	**Bridging law #1 – same extension as for law #3**	$F^f = 30\ N$ $l^f = 12.93\ mm$	193.95	$1100\ J/m^2$
2	**Bridging law #1 – same energy as law #2 (case 3)**	$F^f = 30\ N$ $l^f = 3.09\ mm$	46.35	$625\ J/m^2$
3	**Bridging law #2 – same extension as law #3 (case 4)**	$F^f = 30\ N$ $E^f = 5\ GPa$ $r = 0.1\ mm$ $l^f = 12.93\ mm$	46.35	$625\ J/m^2$
4	**Bridging law #3**	$F^f = 30\ N$ $E^f = 5\ GPa$ $r = 0.1\ mm$	355.58	$1800\ J/m^2$
5	**Bridging law #4**	$F^f = 30\ N$ $E^f = 5\ GPa$ $r = 0.1\ mm$ $d = 5\ mm$	169.95	$1600\ J/m^2$

These cases can be compared to one another. Comparing case 1 and case 2, the energy dissipated by the deformation and breaking of the filament is larger in case 1 than in case 2 due to the higher tensile elongation in case 1, resulting in a higher toughness. The bridging filaments of cases 1 and 3 are characterized by similar properties. However, case 3 consider unfolding of the bridging filament resulting in lower dissipated energy and lower G_{Ic} as consequence and a smoother R-effect. For cases 2 and 3, the resulting toughness is similar as the same energy is dissipated by the breaking of the bridging filaments. However, the filaments are not characterized by the same tensile elongation. In case 2, the tensile elongation is lower and the toughness raises faster than in case 3. The tensile elongation influences thus the distance over which the R-effect is taking place. Case 4 can be compared to case 1 as the fibers are characterized by similar properties. However, in case 1, the force applied on the fiber only acts parallel to it while in case 4, it acts at angle α with respect to the horizontal. Hence, the tensile force acting on the fiber is lower than the macroscopic load. Consequently, the macroscopic load can be increased up to 55 N resulting in more energy dissipated by the bridging filament and a higher fracture toughness. However, in both cases, the maximum fracture toughness is reached for a similar crack length which governs the beam deflection at the filament position. In cases 4 and 5, a lower amount of energy is dissipated by the filament in case 4 and its tensile elongation is much lower resulting in a lower G_{Ic} and a steeper R-effect, in agreement with the previous comparisons. For case 5, the decohesion length *d* influences the results as the shorter *d*, the lower the tensile elongation but the macroscopic load at failure is not affected. Increasing *d* results thus in a higher fracture toughness. These examples showed that to be able to extrapolate or fit experimental results using a bridging model, three main parameters are important:

- The energy dissipated by one fibre: for a given F^f, similar G_{Ic} values are attained for a given amount of energy dissipated by bridging.
- The tensile elongation of the fibre controls the crack propagation length over which G_{Ic} increases, the shorter, the steeper the increase.
- The bridging event: depending on the bridging phenomenon (law), the two above mentioned parameters are influenced.

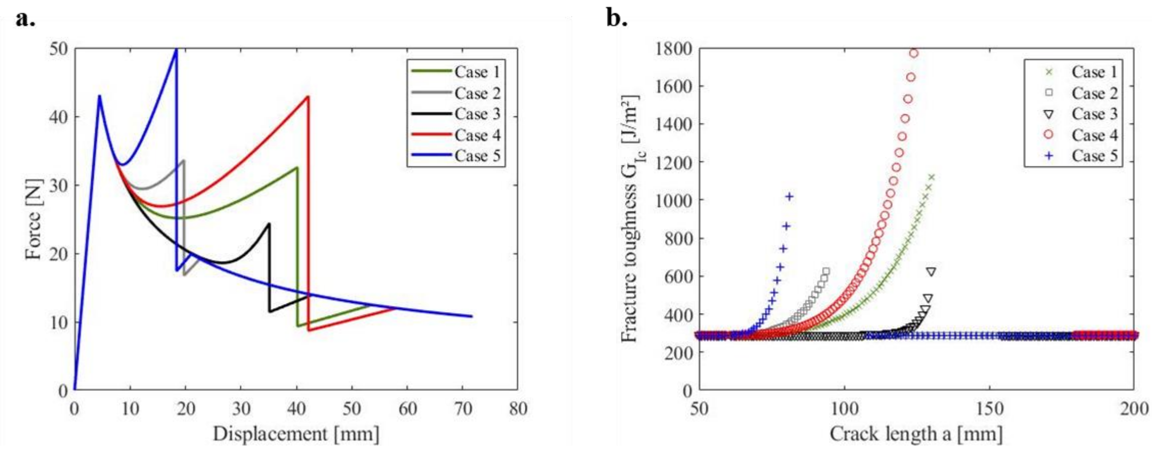

Figure S2.6: a. Force-displacement curves and b. R-curves for the five cases of Table S2.1.

C. S3: Identification of fitting parameters of experimental results

The experimental results for the joints made of *Caperlan TX4 60µm* fishing lines spaced by 1 to 10 mm are already shown in Figure 10. Figure C1 and C2 show the fitting of the experimental results for the other fishing lines spaced by 1 and 2 mm, respectively.

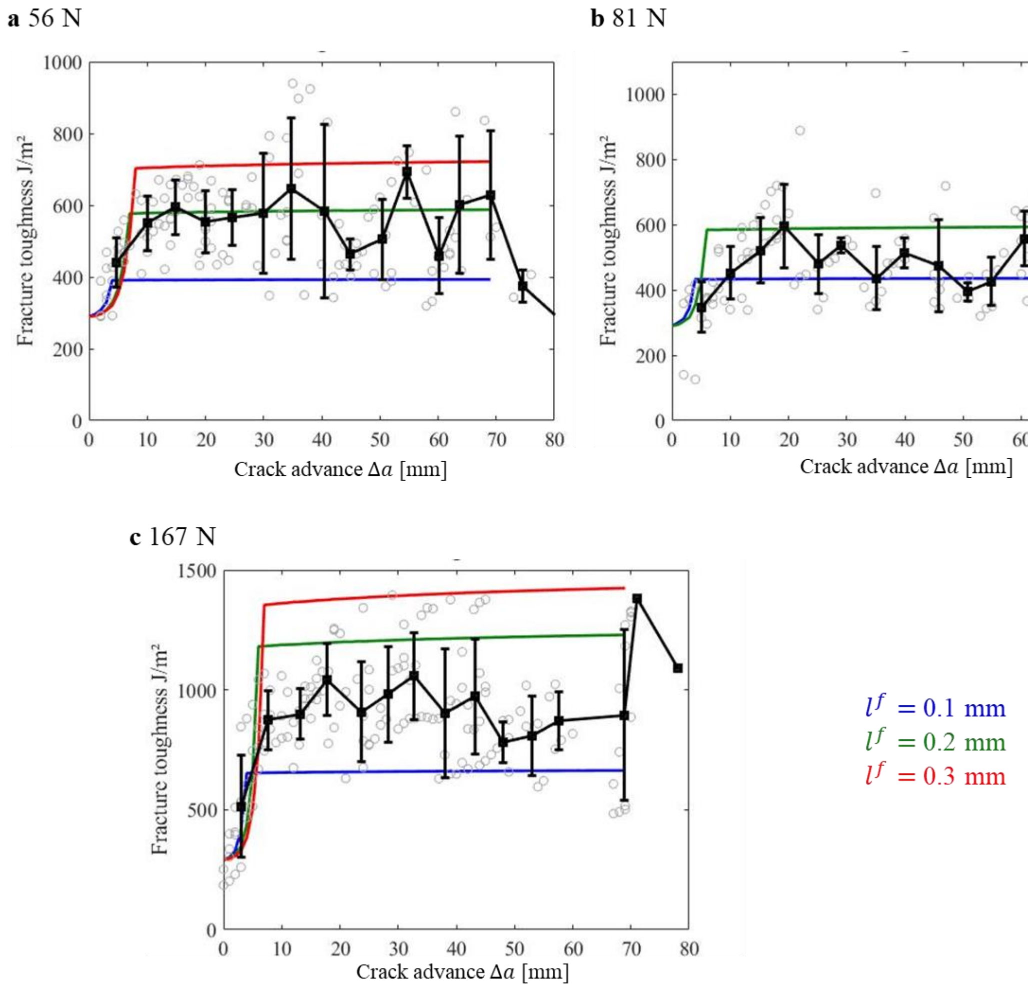

Figure C1: Fitting of experimental results (grey dots and dark line) using the 1st bridging law for different a spacing of 1 mm and UTFs of a) 56 N, b) 81 N and c) 167 N.

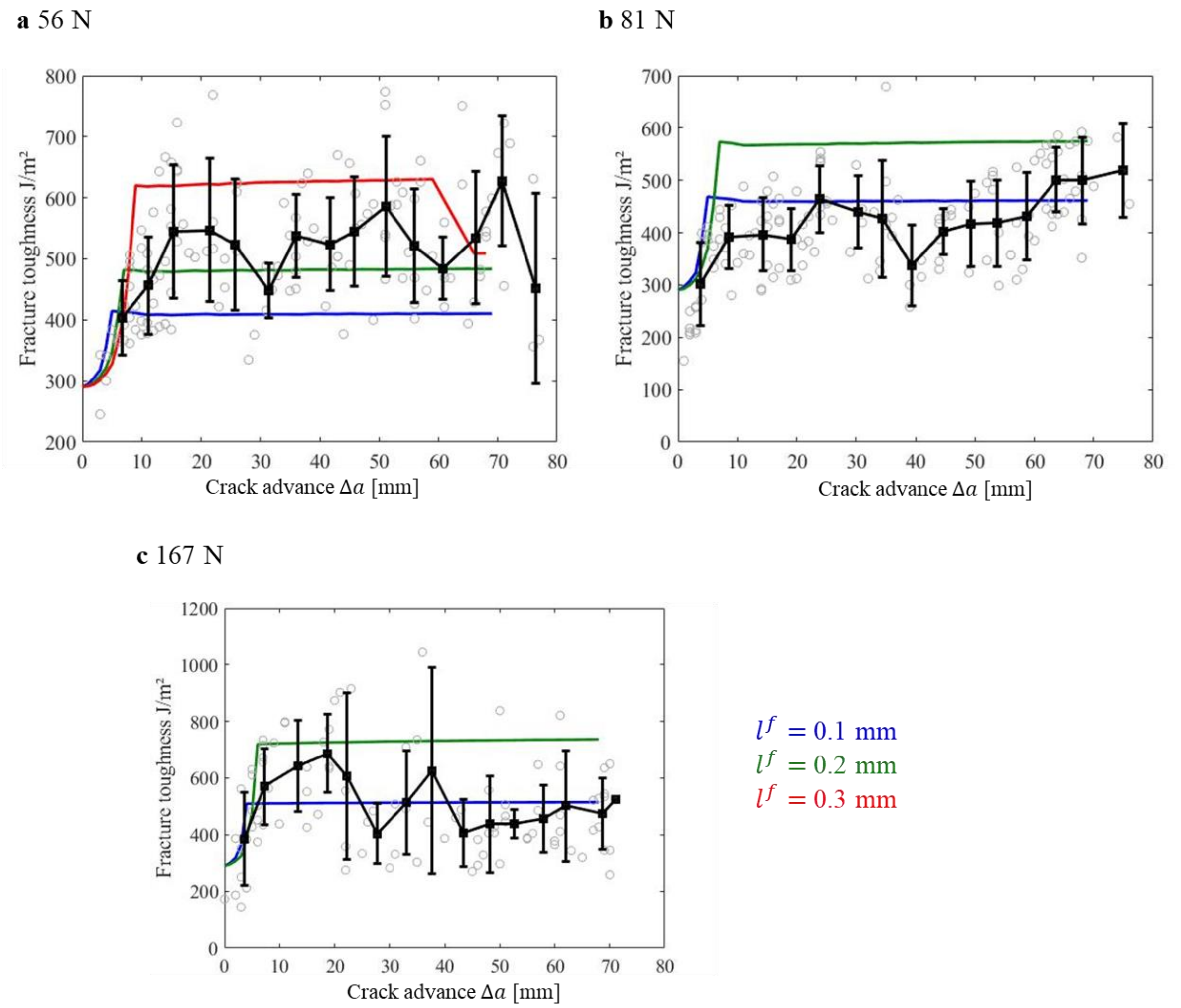

Figure C2: Fitting of experimental results (grey dots and dark line) using the 1st bridging law for different a spacing of 2 mm and UTFs of a) 56 N, b) 81 N and c) 167 N.

The parameter l^f is also used to fit the experimental fracture toughness. Although, a fit of the R-behaviour is not really observed. For all conditions, the tensile elongation is almost the same and ranges between 0.1 and 0.3 mm, indicating that the deposition method using the spikes board leads to reproducible results in this case while for the hand lay-up technique, a larger scattering is observed as observed in Figure 10 when comparing the l^f ranges. In addition, hand lay-up deposition results in longer bridging filaments. Hence, the deposition method could have an influence on the l^f parameter, but this parameter remains difficult to control.

D. S4: Relative toughening effect number

Carpinteri and co-workers (Accornero et al., 2022; Carpinteri, 1984) derived an non-dimensionnal number. By analogy, a non-dimensional number referred as to the relative toughening effect is derived. The brittles number of Carpinteri and co-workers is given by $N_p = \frac{\sigma^f b^{1/2}}{K_{Ic}} \frac{A_s}{A}$ with σ^f being the tensile strength of the reinforcing fibre, b the sample width, K_{Ic} the matrix fracture toughness and A_s/A the proportion of fibres in the sample. The lower this number, the lower the toughening effect and if its value is below a critical value, unstable crack propagation takes place. Following a development like the one of Carpinteri following Equation 2 of the manuscript and considering only a single bridging filament, it is possible to determine the effective bending moment leading to failure:

$$M^f = P^f a = \sqrt{G_0 BEI} + F^f (a - L_1) \qquad (S4.1)$$

$a - L_1$ is equal to the bridging zone length l_b . Equation S4.1 writes thus as

$$M^f = P^f a = \sqrt{G_0 BEI} + F^f l_b \qquad (S4.2)$$

Dimensional analysis gives us

$$\frac{M^f}{\sqrt{G_0 BEI}} = 1 + \frac{F^f l_b}{\sqrt{G_0 BEI}} = 1 + N^p_{n=1} \qquad (S4.3)$$

l_b is unknown and depends on a, l^f, E, B, h and F^f and is difficult to approximate analytically. To consider the fact that we can have several bridging fibres in the bridging zone, we introduce the term l_b/λ representing a density of bridging fibres within the bridging zone, to obtain the brittleness number depending on the number of ligaments,

$$N^p_n = \frac{F^f l_b}{B\sqrt{G_0 E h^3}} \frac{l_b}{\lambda} = \frac{F^f l_b^2}{B\lambda\sqrt{G_0 E h^3}} \qquad (S4.4)$$

. l_b is unknown but it increases if E, b, h and l^f increase or if G_0 and a increase. Consequently, the toughening effect increases if F^f, l^f, B, h or E increases or if G_0 or λ increases, in agreement with the conclusions drawn in Section 5.

References

Bertholet, Y., Olbrechts, B., Lejeune, B., Raskin, J.P., Pardoen, T., 2007. Molecular bonding aided by dissipative inter-layers. Acta Mater. 55, 473–479. https://doi.org/10.1016/j.actamat.2006.08.036

Dépinoy, S., Strepenne, F., Massart, T.J., Godet, S., Pardoen, T., 2019. Interface toughening in multilayered systems through compliant dissipative interlayers. J. Mech. Phys. Solids 130, 1–20. https://doi.org/10.1016/j.jmps.2019.05.013

Li, X., Lu, S., Lubineau, G., 2021. Snap-back instability of double cantilever beam with bridging. Int. J. Solids Struct. 233, 111150. https://doi.org/10.1016/j.ijsolstr.2021.111150

Quan, D., Alderliesten, R., Dransfeld, C., Murphy, N., Ivanković, A., Benedictus, R., 2020. Enhancing the fracture toughness of carbon fibre/epoxy composites by interleaving hybrid meltable/non-meltable thermoplastic veils. Compos. Struct. 252. https://doi.org/10.1016/j.compstruct.2020.112699

Quan, D., Farooq, U., Zhao, G., Dransfeld, C., Alderliesten, R., 2022. Co-cured carbon fibre/epoxy composite joints by advanced thermoplastic films with excellent structural integrity and thermal resistance. Int. J. Adhes. Adhes. 118, 103247. https://doi.org/10.1016/j.ijadhadh.2022.103247

Quan, D., Ma, Y., Yue, D., Liu, J., Xing, J., Zhang, M., Alderliesten, R., Zhao, G., 2023. On the application of strong thermoplastic–thermoset interactions for developing advanced aerospace-composite joints. Thin-Walled Struct. 186, 110671. https://doi.org/10.1016/j.tws.2023.110671

Reedy, J.D., 2008. Effects of patterned nanoscale interfacial roughness on interfacial toughness: A finite element analysis. J. Mater. Res. 23, 3056–3065. https://doi.org/10.1557/JMR.2008.0369

Spearing, S.M., Evans, A.G., 1992. The role of fiber bridging in the delamination resistance of fiber-reinforced composites. Acta Metall. Mater. 40, 2191–2199. https://doi.org/10.1016/0956-7151(92)90137-4

Voleppe, Q., Ballout, W., Velthem, P. Van, Bailly, C., Pardoen, T., 2021. Enhanced fracture resistance of thermoset / thermoplastic interfaces through crack trapping in a morphology gradient. Polymer (Guildf). 218, 123497. https://doi.org/10.1016/j.polymer.2021.123497